Available online at www.sciencedirect.com

SCIENCE DIRECT®

Journal of Solid State Chemistry 177 (2004) 4047–4057

JOURNAL OF SOLID STATE CHEMISTRY

www.elsevier.com/locate/jssc

The effects of synthesis pH and hydrothermal treatment on the formation of zinc aluminum hydrotalcites

J. Theo Kloprogge*, Leisel Hickey, Ray L. Frost

Inorganic Materials Research Group, School of Physical and Chemical Sciences, Queensland University of Technology, 2 George Street, GPO Box 2434, Brisbane QLD 4001, Australia

Received 30 November 2003; received in revised form 20 May 2004; accepted 13 July 2004

Abstract

Zn/Al hydrotalcites were synthesized by coprecipitation at increasing pH from 6.0 to 14.0, followed by hydrothermal treatment at 150 °C for 7 days. The materials were characterized by X-ray diffraction (XRD), STEM, inductively coupled plasma–atomic emission spectroscopy (ICP–AES), thermal analysis, infrared spectroscopy and Raman spectroscopy. The XRD analysis for the samples prepared between pH 9.0 and 12.0 showed a pattern typical of hydrotalcite, with a *c*-axis distance of ~22.6 Å. STEM showed that the pH of preparation affected the stability of the hydrotalcite and that instability, observed at pH 9.0, favored the formation of mixed phases when treated hydrothermally. It was also shown that treatment of a stable starting material increased the crystallinity and resulted in the formation of hexagonal plate-shaped particles. ICP–AES and thermal analysis showed that the Zn/Al ratio and thermal stability increased with pH. Thermal analysis showed three major weight losses corresponding to the loss of interparticle water, interlayer water and dehydroxylation of the hydroxide layers and decarbonization of the interlayer region.

1. Introduction

Anionic clays, such as hydrotalcites, are not as well known and are rarer in nature compared to cationic clays such as smectites. The first hydrotalcite was discovered in Sweden around 1842 [1]. Anionic clays have a structure electrically opposite to that exhibited by cationic clays. Their structure can be derived from the brucite structure, $Mg(OH)_2$, where each Mg^{2+} ion is octahedrally surrounded by six OH^- ions. The hydrotalcite-type (HT) structure is obtained when some of the Mg^{2+} ions, or other divalent cations, are replaced by trivalent cations, with a similar radius [2]. The higher charge of the trivalent cations imposes an overall positive charge on the brucite-type layer, which is compensated by the incorporation of generally hydrated interlayer anions.

A wide range of compositions are possible for synthetic hydrotalcites, based on the general formula $[M^{2+}_{1-x}M^{3+}_x(OH)_2]^{b+}[A^{n-}]_{b/n}\cdot mH_2O$, where M^{2+} and M^{3+} are the divalent and trivalent cations in the octahedral positions within the hydroxide layers, with x normally ranging between 0.17 and 0.33, A^{n-} is an interlayer anion with a negative charge n, b is the charge of the layer and m is the number of water molecules. Many anions or anionic complexes, both organic and inorganic, can and have been incorporated into the hydrotalcite structure. The wide range of materials of this type that can be synthesized gives rise to a range of applications including catalysts and catalyst precursors, ion exchangers and adsorbers, anion scavengers and stabilizers, etc. [3,4].

Several factors are important in the precipitation of HT compounds, such as the nature of the cations, their ratio, the nature of the anions, pH, temperature, aging, and the precipitation method. Although generally anionic clay particles are larger than their counterpart, the cationic clays, there is still interest in the ability to

---

*Corresponding author. Fax: +61-7-3864-1804.
E-mail address: t.kloprogge@qut.edu.au (J.T. Kloprogge).

0022-4596/$ - see front matter
doi:10.1016/j.jssc.2004.07.010

increase particle size, to improve their chemical and physical properties.

A recent study has shown that the carbonate anion concentration in the interlayer region of hydrotalcite was affected by both temperature and aging [5]. It was shown that the best crystalline material was obtained at 25 °C, with at least 5 h of aging. Generally, it is accepted that a basic pH is required for the preparation of hydrotalcites. However, the optimal pH depends on which cations are used and where their hydroxide precipitation curves cross. The crystallinity of the precipitated hydrotalcite can be further increased by hydrothermal treatment [6,7]. In 1980, Miyata showed that using a higher temperature, 180 °C, for hydrothermal treatment increased the crystallite size [8]. Several studies have reported on the influence of the synthesis parameters and show that pH is the major factor in the formation of Zn/Al hydrotalcite [9–13]. Zn/Al hydrotalcites have been used for anion exchange reactions, pillaring and absorption [14–24] and a number of catalytic applications, either with the hydrotalcite structure or after calcination as the mixed metal oxide [25–32].

This study forms part of an ongoing investigation on the effects of reaction conditions during synthesis and hydrothermal treatment of the hydrotalcite minerals with various cations and anions to improve their physical and chemical properties. The aim of this study is to obtain insight into the nature of the Zn/Al hydrotalcite-type materials when the experimental conditions are varied. Samples were prepared over a wide pH range, and the reagent addition was optimized. Samples were selected, based on their purity, stability and crystallinity, and treated hydrothermally to investigate (1) the effects of aging under the influence of temperature, pressure and time, and (2) the effects of pH of preparation on the crystallinity of the hydrothermally treated hydrotalcite.

2. Experimental

2.1. Preparation

Zn/Al hydrotalcites were synthesized by the coprecipitation method, based on a theoretical composition of $Zn_6Al_2(OH)_{16}(CO_3)\cdot 4H_2O$ [33]. Two solutions were prepared, solution 1 contained 2 M NaOH and 0.125 M Na_2CO_3, solution 2 contained 0.75 M Zn^{2+} [$Zn(NO_3)_2\cdot 6H_2O$] along with 0.25 M Al^{3+} [$Al(NO_3)_3\cdot 9H_2O$]. For sample 1, solution 2 was added to solution 1; for sample 2, solution 1 was added to solution 2. The pH was maintained at ~12, for both methods. The best method was established on the basis of crystallinity and purity. Using the optimum method, the next series of samples were prepared by varying the pH from 6.0 to 6.5, 9.0, 9.5, 10.0, 10.5, 11.0, 11.5, and >14, and labelled 3–10. In all experiments, solutions were added using a peristaltic pump at a rate of 40 mL/min, under vigorous stirring. The pH was maintained constant by adding HNO_3 when necessary. When the addition was complete, the mixture was stirred for a further 1.5 h, during which time the pH was still maintained constant. Two samples were selected based on their purity, stability and crystallinity, and were treated hydrothermally at autogenous water vapor pressure at 150 °C, in Teflon-lined stainless steel Parr Bombs for 7 days (samples 11 and 12). All samples were filtered, thoroughly washed several times, in approximately 500 mL of deionized water each time to remove excess soluble ions, and finally the samples were oven dried at 60 °C for 1 h.

2.2. Characterization

2.2.1. Powder X-ray diffraction (XRD)

Powder XRD (XRD) diagrams were recorded on a Phillips wide-angle PW 1050/25 vertical goniometer equipped with a graphic diffracted beam monochromator. The *d*-values and intensity measurements were improved by application of an in-house developed computer-aided divergence slit system enabling constant sampling area irradiation (20 mm long) at any angle of incidence. The radiation applied was Co$K\alpha$ from a long fine-focus Co tube operating at 40 kV and 40 mA. The samples were measured in the step-scan mode from 5 to 75°2θ, with steps of 0.02°2θ and a counting time of 2 s. Jade software package (Materials Data, Inc.) was used to analyze the data; identification of the existing crystalline phases was based on comparison with preexisting JCPDS diffraction data files. Pattern manipulation and interpretation were performed using TracesV4 (Diffraction Technology Pty. Ltd.) and Microsoft EXCEL.

2.2.2. Transmission electron microscopy (TEM)

Electron micrographs of the samples were taken by the TEM method at 200 kV with a Philips CM200 Analytical Scanning TEM instrument, equipped with LaB6 filament, cryo vacuum options, and link thin-window Si EDS detector. Microanalysis of selected samples was carried out in the STEM mode using an energy-dispersive X-ray spectrometer with Link ISIS system. Samples were prepared by suspension in alcohol (70%) and a small amount was placed on a carbon-coated copper grid, prior to use in the TEM.

2.2.3. Inductively coupled plasma–atomic emission spectroscopy (ICP–AES)

ICP–AES was used for elemental analysis of the Zn and Al ions. A calibration series of standards for determining the relative amounts of Zn and Al were prepared at 10, 50, 100, and 200 ppm. Small amounts of the samples were accurately weighed and digested in 3 mL of 6 M HCl along with 1 mL of 6 M HNO_3. The relative amounts of each atom were recorded on Varian Liberty 2000 ICP–AES at wavelengths of 394.40 and 213.86 nm for Al and Zn, respectively.

2.2.4. Thermal analysis

Differential thermal analysis (DTA) and thermal gravimetric analysis (TG) of the samples were recorded on a Setaram 2000 (1992) unit. The samples were measured under a stream of argon (20 mL/h) at a heating rate of 2°/min, from 30 °C to 1000 °C at a heating rate of 2°/min. Data manipulation and interpretation was carried out using Microsoft EXCEL.

2.2.5. Fourier transform infrared (FTIR) and Raman spectroscopy

FTIR spectra were recorded using the KBr tablet technique (2 wt% sample) on a Perkin-Elmer FT-IR 1000 spectrometer; 64 scans were taken to improve the signal-to-noise ratio in the range of 400–4000 cm^{-1}, the normal resolution was 4 cm^{-1}. The Raman spectra were obtained using a Renishaw 1000 Raman microscope system, which includes a monochromator, a filter system and a charged-coupled device (CCD) as the detector. Raman spectra were excited on a Spectra-Physics model 127 He/Ne laser (633 nm), scanned for 15 s for 1000 scans and recorded in the range of 400–1800 and 2800–4000 cm^{-1}. Data manipulation, such as baseline adjustment, smoothing and normalizing as well as interpretation, was performed using the Spectracalc software package GRAMS (Galactic Industries Corporation, NH, USA) and Microsoft EXCEL. Band component analysis was undertaken using the Jandel "Peakfit" software package, which enabled the type of fitting function to be selected and allowed specific parameters to be fixed or varied accordingly.

3. Results and discussion

3.1. Effect of reagent addition

The XRD patterns of all samples are shown in Fig. 1. The crystalline components in samples 1 and 2 (pH 12) show some significant differences. Both show a sharp symmetric (003) reflection at low 2θ angles corresponding to a c-axis of ~22.8 Å. Both spectra also show broad asymmetric peaks at higher angles, which are characteristic of clay minerals possessing a layered structure and are similar to the pattern of natural hydrotalcite [7,34]. Sample 1 (pH 12), however, shows additional peaks that are associated with the second major phase zincite (ZnO) and sodium nitrate ($NaNO_3$) as a minor phase. The difference in the crystalline products formed is due to the variation in synthesis conditions, where based on the Zn solubility curves precipitation of ZnO starts at pH ~9 [35]. The addition of the hydroxide-containing solution to the cations-containing solution yielded a hydrotalcite-type material without the ZnO impurity. Proceeding via this pathway is therefore preferred as it progresses under acidic conditions that do not favor the formation of ZnO [35]. Under strong alkaline conditions, ZnO species are not soluble and compete with the formation of Zn/Al hydrotalcite.

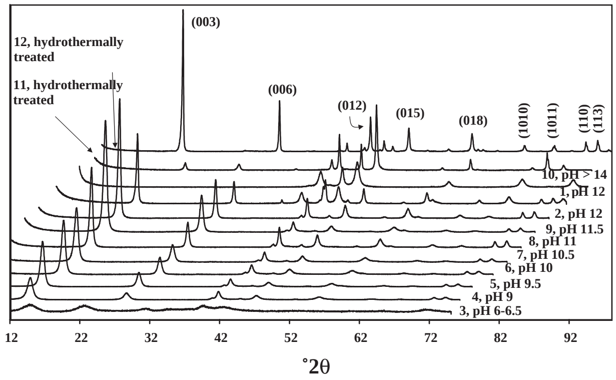

Fig. 1. XRD patterns of all synthetically prepared Zn–Al hydrotalcite samples (1–12) in comparison with each other.

3.2. The effect of pH of synthesis

The pH of preparation is important in the formation of all hydrotalcite-type materials and the optimum pH depends on the cations used (Fig. 1). Sample 3 (pH 6.0–6.5) displays very weak, broad peaks at higher 2θ values (14.9°) compared to sample 2 (pH 12, 13.6°). The XRD patterns of sample 3 (pH 6.0–6.5) show that no hydrotalcite structure is formed under acidic synthesis conditions. The broadness of the peaks indicates that the sample is poorly crystalline, where the reflections occur at similar 2θ values as for brucite, indicating that a low crystalline hydroxide similar to brucite is formed instead of hydrotalcite. Samples prepared within the pH range of 9.0–12.0 (samples 4–9 and 2) show patterns similar to that of natural hydrotalcite [7], with the (003) reflection corresponding to a c-axis of ~22.5 Å. The difference between these samples is in the intensity of the (00l) reflections. As pH increases, from 9.0 to 12.0, the intensity of the reflections increases and the line width decreases, corresponding to an increase in crystallinity. Samples 2 and 9 at pH 12 and 11.5, respectively, have the most intense and sharpest peaks, and thus are the most crystalline samples. Sample 10 (pH > 14) shows a structure different from the previous samples; it is composed of one major crystalline phase being ZnO and a minor phase, sodium nitrate. Based on solubility curves and predominance diagrams for Zn^{2+}, at this strong alkaline pH, zinc-hydroxy complexes, such as hydrotalcites, become more soluble and ZnO, the predominant phase that would be precipitated. It is concluded that the hydrotalcite phase formed at lower pHs during synthesis would redissolve at this high pH to form ZnO [35].

The TEM of sample 5 (pH 9.5) shows large particles, 120 nm across, with a distorted hexagonal shape (Fig. 2a). The particle morphology was observed to be regular and homogenous throughout. The electron diffraction pattern appeared very weak and the beam exposure was destructive to the sample. The STEM analysis exhibits a bulk ratio of Zn/Al of ~2.1 for a cluster of crystals. This analysis also shows that a small amount of nitrogen is present; however, the signal was very weak and the crystalline phase could not be identified in the TEM mode. Sample 9 (pH 11.5) shows large particles of ~180 nm across. The particle shape of this sample was almost hexagonal and regular throughout the sample. This sample displayed a ratio of Zn/Al = 2.6.

The TEM of sample 10 (pH > 14) is primarily composed of rounded, elongated, flat crystals of submicron size (27–58 nm). The particle shape is regular and the diffraction pattern was very strong, indicating a highly crystalline phase (Fig. 2b). The STEM analysis showed that Zn and O are the major components, and that Al is only present in a trace amount (1/20). This is in agreement with the XRD that indicated only ZnO with a minor trace of sodium nitrate as the crystalline component.

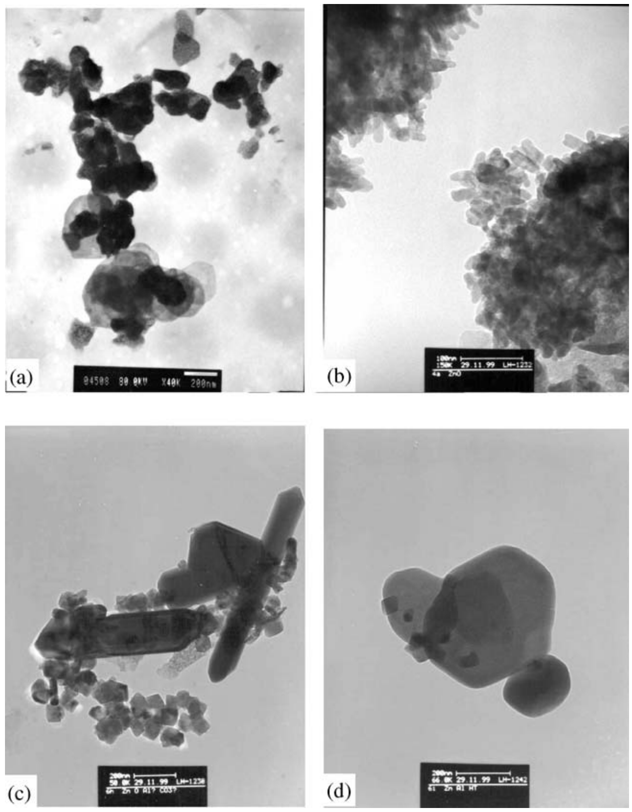

Fig. 2. TEM images of Zn/Al hydrotalcites: (a) sample 5, (b) sample 10, (c) hydrothermally treated sample 11 and (d) hydrothermally treated sample 12.

Table 1
Chemical composition of Zn/Al for samples 2, 4–9 with increasing synthesis pH

Sample	ICP-AES analysis (ppm)		Sample mass in 200 mL (g)	Concentration ratio Zn/Al
	Al	Zn		
4 (pH 9)	17.47	80.40	0.0509	1.89
5 (pH 9.5)	15.75	81.03	0.0523	2.11
6 (pH 10)	14.44	74.73	0.0490	2.13
7 (pH 10.5)	16.01	81.95	0.0516	2.11
8 (pH 11)	14.04	73.49	0.0487	2.14
9 (pH 11.5)	16.87	83.92	0.0485	2.16
2 (pH 12)	14.76	80.47	0.0498	2.25

Table 1 summarizes the chemical composition derived from the ICP–AES analyses for samples 2, 4–9 (pH 12, 9–11.5), with a precision of ~5%. The Zn/Al ratio ranges from 1.89 (sample 3, pH 6–6.5) to 2.25 (sample 9, pH 11.5), and differs from the ratios obtained from STEM as they are bulk ratios. It is apparent that, whilst expecting a theoretical ratio of 3, all samples have a ratio of ~2, which is in accordance with the findings of Velu et al. [36] and Roussel et al. [37,38] for Zn/Cr hydrotalcite. It is postulated that the lower ratio observed in both studies is due to preferential crystallization of Zn-hydrotalcite as $Zn_4Al_2(OH)_{10}(CO_3) \cdot xH_2O$, rather than a hydrotalcite with a Zn/Al ratio of 3:1. Previous studies have indicated that the possible formation of hydrotalcites involves the reaction of a solution containing the divalent metal with the trivalent metal hydroxide [13]. This would explain the results obtained with samples 1 and 2 (pH 12). It also would explain the increase in crystallinity with the pH. The pH range between 9.0 and 12.0 is considered to be ideal for the preparation of hydrotalcites, and is a commonly used range for their synthesis.

The DTA/TGA patterns of representative samples are shown in Fig. 3. The hydrotalcite samples 5 and 9 (pH 9.5 and 11.5) show similar features in both patterns. The TGA curve does not exhibit well-defined plateaus between the decomposition steps, which extend over relatively high temperature ranges. However, in light of the DTA pattern, two major weight losses can be identified, which is in agreement with the well-known decomposition mechanism of such compounds, which predicts two distinctive steps of weight loss [39–41]. The first weight loss occurs around 200 °C and reflects the loss of physically adsorbed (surface) and interlayer water [36,42,43]. The loss of surface water begins as soon as heating commences and is completed at ~90 °C,

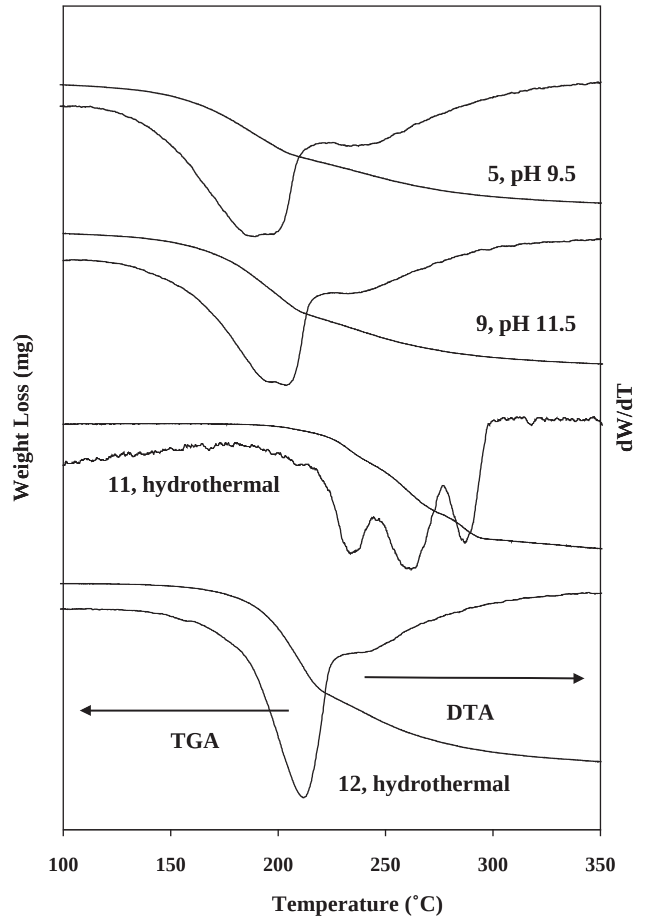

Fig. 3. Thermal analysis of Zn/Al hydrotalcite of samples 5, 9, 11, and 12: (a) TGA, (b) DTA.

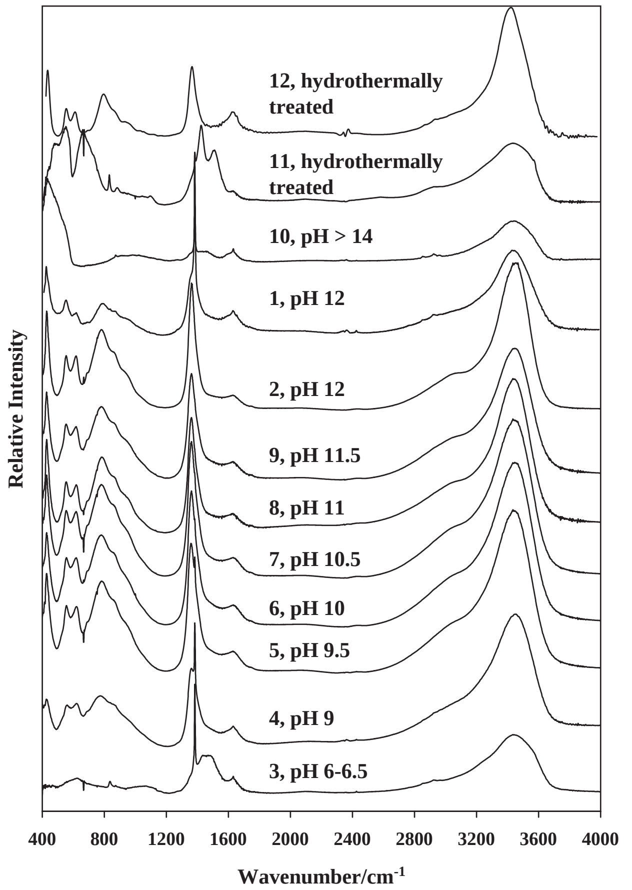

Fig. 4. FT-IR spectra of all synthetically prepared samples (1–12), showing the effects of pH and hydrothermal treatment.

the removal of the interlayer water is finished at ~190 °C. TGA-MS study of Mg/Al-hydrotalcite has shown that up to 200 °C water is lost in several steps, accumulating in a major loss around 195 °C [44]. The decomposition step, starting at ~200 °C, is due to the decomposition (dehydroxylation) of the hydroxide layers and the removal of interlayer anions (carbonate) [44]. The end products of the thermal decomposition have been shown to be metal oxides as well as mixed-oxide spinel-type phases [43,45]. The patterns of various samples differ with respect to the temperature at which the weight losses occur, such that sample 5 (pH 9.5) occurs at a lower temperature than for sample 9 (pH 11.5). Since stability is dependant on temperature, sample 9 appears to be the most stable sample from this series [46]. It is concluded, in comparison with the XRD and TEM results, that the more crystalline samples have the highest thermal stability.

The FT-IR spectra for samples synthesized at various pH conditions are shown in Fig. 4, and their assignment in Table 2. With the infrared assignment, it has to be kept in mind that most of the OH groups are (when not at the edges of the crystals) triply coordinated to the di- and trivalent cations [33]. If the various metals in the hydrotalcites (Zn, Al) are distributed at random, it is unlikely than an OH group is surrounded by three metal cations of the same kind, especially Al_3OH. In most cases, one OH group will be coordinated by the two different metal cations. In the following sections, the vibrations will be assigned to the coordination which it most likely resembles, e.g. “Al-OH”. All spectra show a very broadband between 2700 and 3750 cm^{-1}. Band component analysis (Fig. 5) reveals three superimposed peaks at 3025, 3348, and 3468 cm^{-1}. The 3025 cm^{-1} band is generally interpreted as the CO_3–H_2O bridging mode [7,47]. The 3348 cm^{-1} band is ascribed to the H-bonded interlayer H_2O surrounding the anions. The strong band at 3468 cm^{-1} is assigned to the metal-OH-stretching mode. However, the various metals (Zn, Al) bonded to the OH group cannot be distinguished between themselves [48].

Within the range of pH synthesis conditions, the positions of the infrared bands change up to 50 cm^{-1} and generally the intensity increases with increasing pH. In addition, peaks become sharper with increasing pH. Since increasing intensity corresponds to an increase in the order, the samples prepared at pH 11.5 and 12 are the most crystalline and the sample prepared at pH ~6.5

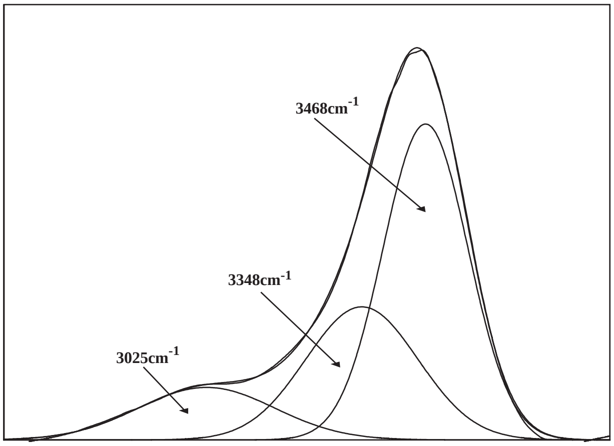

Fig. 5. Band component analysis of the OH-stretching region for the infrared spectrum, of synthetic Zn/Al hydrotalcite sample 2.

is the least crystalline. All samples have a weak broad peak centered ~1630 cm^{-1}. This peak is associated with the deformation mode of water (ν_2).

Samples 2, 4–9, and 12 (pH 12, 9–11.5 and hydrothermally treated) show a peak centered ~1400 cm^{-1} in the infrared spectrum, associated with the presence of CO_3^{2-} species in the interlayer region. Assuming the carbonate species is present as the free ion (D_{3h}) and not specifically involved in any bonds, only three bands should be present in the infrared spectrum, ν_2, ν_3 and ν_4 [49,50]. Comparison of the spectrum carbonate modes with that of the free ion discloses a shift to lower wavenumbers, which is due to the interaction of the carbonate ions with the water molecules in the confined space between the hydroxide layers resulting in loss of freedom, therefore leading to a lowering of the carbonate symmetry to C_{2s} or C_v [48]. The out-of-plane bending mode (ν_2) and in-plane bending mode (ν_4) are usually found at 874 and 680 cm^{-1}, respectively. Close examination of the spectra reveals the activation of the symmetric stretching vibration, ν_1, as a very weak shoulder band at ~1045 cm^{-1}, which is overlapped by the metal-OH translational modes. The lowering of symmetry is further confirmed by the splitting of the ν_3 mode.

In certain samples, the ν_3 antisymmetric stretching mode at ~1400 cm^{-1} has a sharp peak at high intensity, with a broad base at low intensity. Band component analysis of sample 4 prepared at pH 9.0 shows the presence of three overlapping bands: one sharp and two broader bands (Fig. 6a). The broader bands at 1359 and 1399 cm^{-1} are assigned to the antisymmetric stretching mode (ν_3) of the CO_3^{2-} species. The sharper band at 1384 cm^{-1} is assigned to nitrate, as nitrate always gives a very sharp and intense peak around this frequency. It should be noted that with increasing pH the presence of nitrate is no longer observed. The presence of nitrate in the interlayer region of the hydrotalcite is caused by the fact that metal nitrates were used to synthesize the hydrotalcites. Band component analysis of sample 2 (pH 12) shows only two broad peaks at 1361 and 1397 cm^{-1} corresponding to the splitting of antisymmetric stretching mode, ν_3, of carbonate to ν_3 and ν_{3a} (Fig. 6b). Sample 3 (pH 6–6.5) also show signs of nitrate; however, the carbonate antisymmetric stretching mode has shifted. Sample 3 (pH 6–6.5) shows a very weak broad peak at ~1450 cm^{-1}, which is assigned to carbonate and occurs at a higher wavenumber than for the other samples. XRD has already shown that this sample did not contain any crystalline hydrotalcite, which fits well with the shift in the carbonate band in the infrared spectrum. Sample 10 (pH > 14) is different as it has a very sharp nitrate peak around 1388 cm^{-1} and a very weak, almost indistinguishable carbonate band. Considering that this sample was characterized as to be primarily composed of ZnO, these results are consistent, as no carbonate should be present.

Table 2 gives the infrared band positions, of selected samples between 1000 and 400 cm^{-1} and their assignments. Band component analysis (Fig. 7) shows the complexity of the spectrum in this region, where in most cases a number of overlapping bands exist. The assignment of these bands is consistent with the XRD results, where most samples show a mixture of bands including those of "Zn-OH", "Al-OH", CO_3^{2-} and NO_3^-. Sample 2 (pH 12), for example, clearly shows in this region a pattern typical of hydrotalcite, where it has a broad shoulder at 868 cm^{-1} and strong bands at 553 and 430 cm^{-1} [51]. Sample 10 shows no "Al-OH" translations modes, as was expected.

The examination of the samples using Raman spectroscopy compliments the infrared study [52]. The hydroxyl-stretching region (3000–4000 cm^{-1}) of the spectra is quite broad and very weak. Fig. 8 shows the Raman spectra between 350 and 1600 cm^{-1} of all samples.

The first group of samples 1, 2, 4–9, and 12 (pH 12, 9–11.5 and hydrothermally treated) display an intense peak centered at ~1064 cm^{-1}, assigned to the ν_1 symmetric stretching mode (A_1') of carbonate and the "Al–OH" translation [49]. The antisymmetric stretching mode (E') ν_3 and in-plane bending mode (E') ν_4 usually lie at 1415 and 680 cm^{-1}, respectively; however, they are eminently weak and are unable to be confidently assigned [53]. Sample 3 has two peaks at 1052 and 1077 cm^{-1}, assigned to the nitrate symmetric stretching mode (ν_1) and carbonate symmetric stretching mode, respectively. The frequency of the carbonate symmetric stretching mode has shifted to a higher frequency than the free ion; this is due to the lowering of symmetry from the free ion D_{3h}. Sample 10 (pH > 14) shows a very weak and broad 1068 cm^{-1} peak that cannot be precisely assigned.

At the lower end of the Raman spectrum, samples that contained an identifiable hydrotalcite phase and

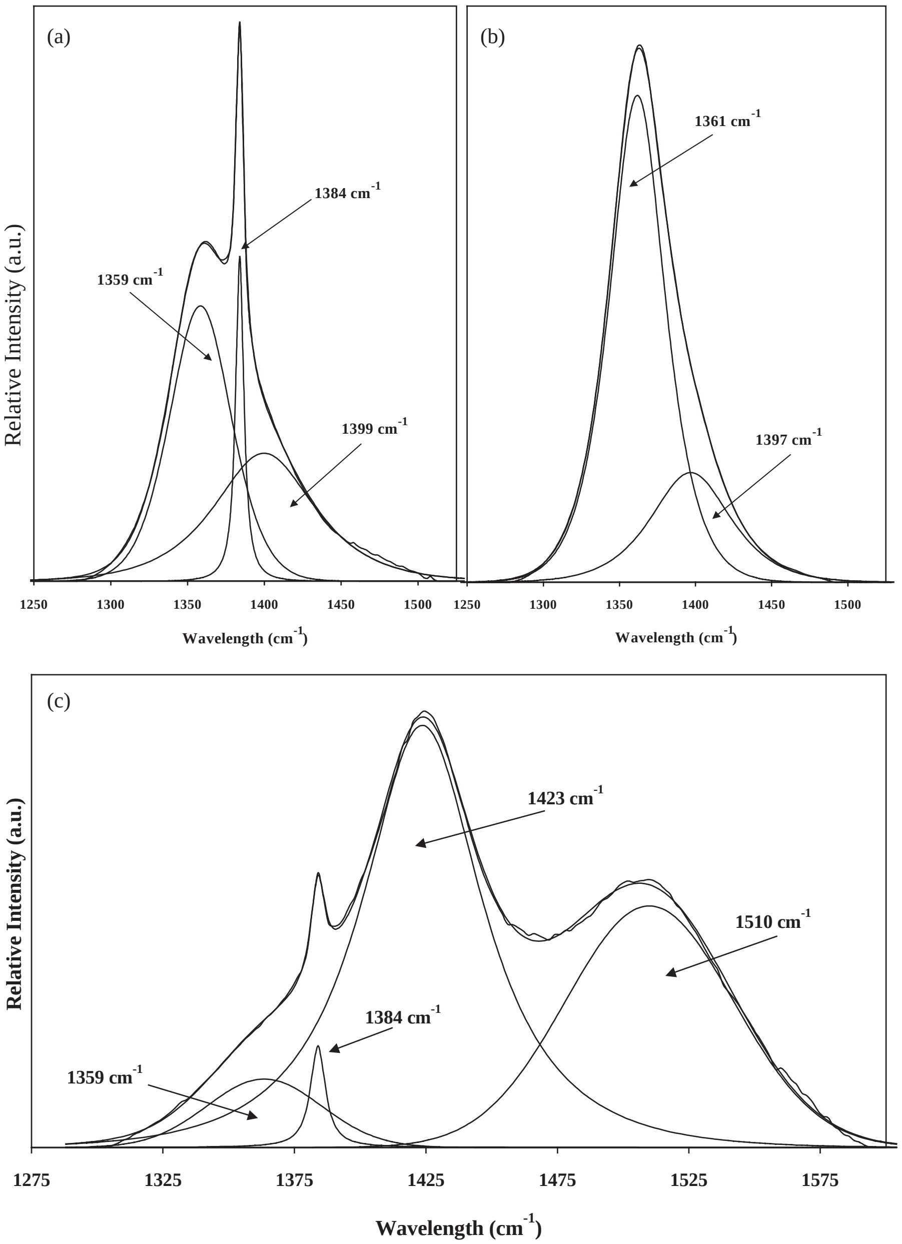

Fig. 6. Band component analysis of the CO_3^{2-} antisymmetric stretching mode (ν_3) in the infrared spectrum of synthetic Zn/Al hydrotalcite samples: (a) 4, (b) 2, and (c) 11.

exhibited similar carbonate infrared active stretching modes (samples 1, 2, 4–9, 12) also have comparable bands in the Raman spectra. The samples show a peak at $\sim$553 cm^{-1} assigned to the "Al-OH" translation mode as well as a peak $\sim$500 cm^{-1} that can be assigned to "Zn-OH" or "Al-OH" translation modes, but is probably a combination of both. Both these peaks have shoulders that are too weak to accurately assign. Sample 3 shows no assignable peaks, consistent with XRD and IR, in this region. Sample 10 (pH$>$14) shows the same peak at 439 cm^{-1} and is more intense and sharper that the former sample. Furthermore, this sample contains no peaks at $\sim$555 cm^{-1} assigned to "Al-OH" as expected.

3.3. The effect of hydrothermal treatment of Zn/Al–Ht

Two samples from the previous pH series were treated hydrothermally; one synthesized at the high pH with good crystallinity (sample 9, pH 11.5) and the other at lower pH with poor crystallinity (sample 5, pH 9.5). Fig. 1 shows that the two hydrothermally treated samples (11 and 12) have different structures. Sample 11 appears to have lost all of the hydrotalcite structure and is composed of one major crystalline phase, ZnO, and two or even three other minor crystalline phases, containing various amounts of Zn^{2+}, Al^{3+}, CO_3^{2-}, and OH^-. The minor phases are associated with the

Table 2
Infrared frequencies and assignments of the various modes of vibrations between 1000 and 400 cm^{-1} [48,49,51]

1 (pH 12)	2 (pH 12)	10 (pH >14)	11 (HT)	12 (HT)	NO_3^-	CO_3^{2-}	Natural HT	Gibbsite ($Al(OH)_3$)	Hydrozincite ($Zn_5(CO_3)_2(OH)_6$)	Zincite (ZnO)	Suggested assignment
950	942			948				958			"Al-OH" deformation
908			883						900–880		"Zn-OH" deformation
			868			879–866					ν_2-CO_3^{2-}
870	868			866			865				ν_2-CO_3^{2-} in a HT
839			833	834	839						ν_2-NO_3^-
791	785			793				800			"Al-OH" translation
747	739							749			"Al-OH" translation
			732						738		"Zn-OH" translation
695			690	690	692						ν_4-NO_3^-
	686			676		680	670				ν_4-CO_3^{2-}
			644						710		"Zn-OH" translation
619	620	617		614						615	"Zn-OH" translation
579	591			587				585			"Al-OH" translation
552	552			553			555	562–540			"Al-OH" translation
		545	557							535	"Zn-OH" translation
518	523	515		521				515	520		"Zn-OH" or "Al-OH" translation
		488	483						460		"Zn-OH" translation
450		440	430							440	"Zn-OH" translation
426	430			435			412	420			"Al-OH" translation
		422									Unknown

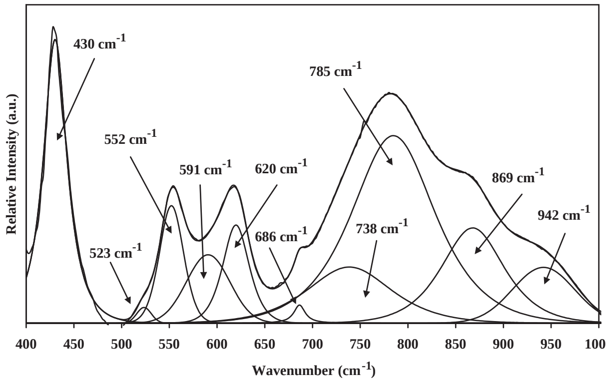

Fig. 7. Band component analysis of the lower frequency region, between 1000 and 400 cm^{-1}, of the infrared spectrum of synthetic Zn/Al hydrotalcite sample 2.

reflections at 15.0 and 22.6°2θ, indicating a small amount of hydrozincite, $Zn_5(OH)_6(CO_3)_2$, and/or zinc carbonate hydroxide hydrate, $Zn_4CO_3(OH)_6 \cdot xH_2O$. The reaction mechanism that plays a major role in the decomposition of the low-crystallinity hydrotalcite is unclear at this stage. Sample 12 yielded a highly crystalline hydrotalcite-type compound, where the peaks are more intense and sharper than the sample from which it was prepared. However, there are several small peaks, which are just resolved that are associated with sodium nitrate.

The TEM of sample 11 (Fig. 2c) shows numerous crystalline phases. The most obvious phase is thick, needle-like and the largest crystal type in this sample. The type is extremely crystalline, exhibiting a strong

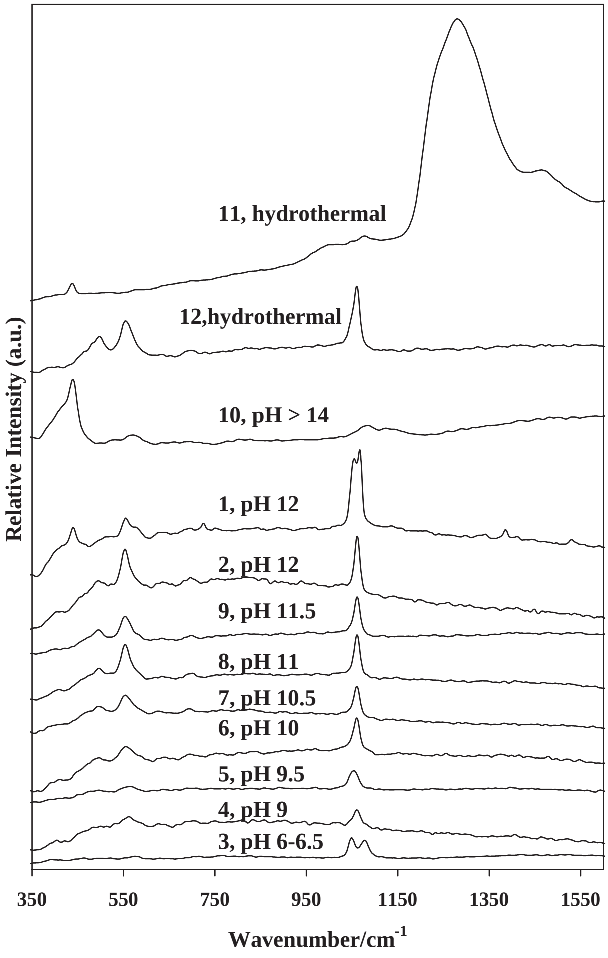

Fig. 8. Raman spectra of samples, showing the changes brought about by pH and hydrothermal treatment.

electron diffraction pattern, and according to the STEM is primarily composed of Zn and O. This phase is assigned to the hydrozincite, even though carbon could not be observed, but the structure is different from the ZnO phase of sample 10 (pH 14). The next phase is structurally similar to the other ZnO phase observed with elongated crystals that are rounded at the top. This phase differs from the first phase in terms of the morphology; it is thinner and edges are rounded, and is composed of Zn and O in a different ratio. This phase is assigned to ZnO. The third phase has a hexagonal shape with a particle size of ~77 nm across. The diffraction pattern is strong and the STEM analysis revealed a ratio of Zn/Al of ~2. The fourth phase is also highly crystalline according to the diffraction pattern, and particles have cubic-type morphology. The particle size is approximately the same as the hexagonal-shaped phase but smaller than the first two phases. This phase is quite common and appears to make up the bulk of the sample, and is primarily composed of Al/Zn with a ratio of 5/4. This was not expected since the XRD showed that no crystalline Al phase was likely to be present. Although this cubic phase makes up the bulk of the sample, the initial two ZnO phases are highly crystalline and exhibit very strong diffraction patterns, which probably suppress the diffraction of the smaller less crystalline phases. The final identifiable phase is a flat flaky structure, which exhibits a diffraction pattern and is also a crystalline phase. The STEM reveals that this phase is composed of Zn, Al, C and O in varying compositions, indicating a hydrotalcite-like phase.

The TEM of sample 12 (Fig. 2d) showed large, flat particles (260 nm) similar to those of the untreated samples. Although the morphology of most particles is fairly regular, there does appear to be another phase. The predominant phase has a distorted hexagonal shape where some of the edges are rounded, similar to sample 9, indicating signs of dissolution during the hydrothermal treatment. The electron diffraction pattern shows a pattern stronger than sample 9. The STEM analysis found a ratio of Zn/Al ratio of 2.5–3.2, compared to an initial ratio of 2.6 in sample 9. The TEM also showed smaller crystals with a cubic morphology, on the rounded surfaces of larger hexagonal-like crystals, which were too small for microanalyses. Thus, hydrothermal treatment increases the crystallinity and allows time for the classical hexagonal shape of the hydrotalcite to form [2,54]. The presence of the smaller cubic-shaped particles indicates that with aging predominant crystal growth occurs on the edges, resulting in relatively thin hexagonal plate-shaped crystals with rounded edges. These smaller particles are believed to be the initial stages of growth of a second phase that was found to be present. This second phase consisted of rounded elongated crystals that are composed of Zn and O, in a ratio of 1:1. It is concluded that these particles grew as a result of the dissolution of the larger hexagonal-shaped, crystalline phases. However, the contribution from this phase to the total sample is small as only a few crystals were observed.

The TGA/DTA of sample 12 is shown in Fig. 3. This sample exhibits similar thermal properties as the two starting samples previously discussed. The primary difference between all these samples is the thermal stability. Sample 12 is the most thermally stable, where all decomposition steps occur at higher temperatures than for the other samples. Furthermore, this sample confirms that the more crystalline samples are the most thermally stable.

The infrared spectrum of sample 11 is eminently different from the hydrotalcite samples (Fig. 4, Table 2). At high frequency (3000–4000 cm^{-1}), a broad feature exists that is assigned to OH-stretching modes. At mid-frequency, several bands are prominent that are assigned to the presence of carbonate. Band component analysis of this region shows the CO_3^{2-} antisymmetric stretching modes are less superimposed, occurring at frequencies of 1423 and 1510 cm^{-1}. These bands occur at different frequencies as they are not residing in the interlayer, as with the hydrotalcites. Instead, it is assumed that carbonate is present in a covalent metal-to-anion bond, Zn–CO_3, where the individual sites occupied by Zn, C and O have symmetries $C_{3I} = S_6$, D_3, and C_2, respectively [20,24]. It is also noticed that they occur at higher frequencies; thus the carbonate species present in this sample is symmetric than those in the hydrotalcites. The band at 1384 cm^{-1} is associated with the presence of nitrate. Furthermore, this sample shows another weak, broad, shoulder peak at 1359 cm^{-1}, which can be assigned to a vibrational mode of hydrozincite, usually found at 1340 cm^{-1}, which is consistent with previous studies [51]. At lower frequency, sample 11 shows a different pattern compared to all other samples. Band component analysis reveals numerous overlapping bands, where the predominant bands are associated with “ZnOH” translational modes (Table 2). Unlike sample 10 (pH > 14), also primarily composed of ZnO, this sample shows CO_3^{2-} and NO_3^- in-plane and out-of-plane bends (ν_4 and ν_2), that are associated with the hydrozincite phase, which lie at higher wavenumbers than for the hydrotalcites.

The infrared spectrum of samples 12 (Fig. 4) is very similar to those of the other hydrotalcites, although there are several weak bands at low frequency that the other hydrotalcites do not show; these bands lie at a frequency associated with nitrate, 834 and 690 cm^{-1}. The primary difference between the spectra of these hydrothermal samples and the untreated samples is in the intensity; such that sample 12 has more intense, sharper and better-resolved peaks than the starting material, sample 9 (pH 11.5), and all other untreated hydrotalcites. This sample has experienced an increase in crystallinity, with treatment [2,54].

The Raman spectrum of sample 11 (Fig. 3) shows an intense, broad peak at 1280 cm^{-1} with a shoulder at 1466 cm^{-1}. In this sample, the carbonate is not present as the free ion. The position of the band is at a higher wavenumber than the other hydrotalcite samples; thus, this peak is assigned to a carbonate species with a lower symmetry than the other samples and the free ion. The band component analysis of this region shows four bands at 1222, 1265, 1319, and 1458 cm^{-1}. These bands are associated with carbonate symmetric and antisymmetric stretching modes, v_1 and v_3. The peaks at 1265 and 1319 cm^{-1} are the v_1 symmetric stretching modes and 1222 and 1468 cm^{-1} are the v_3 antisymmetric stretching modes. The antisymmetric stretching modes are assigned to the weaker, broader peaks, as typically these modes are difficult to assign in the Raman spectrum [53]. This sample has another small peak at 1058 cm^{-1} that is assigned to the nitrate symmetric stretching mode, v_1. At the lower end of the spectrum, this sample shows the same "Zn-OH" translational peak at 438 cm^{-1}, but, however, no identifiable "Al-OH" peak, as it is probably too weak. Sample 12 shows features similar to the other hydrotalcites, but, however, is more ordered, as the peaks are more intense and sharper.

4. Conclusion

XRD, STEM, ICPAES, thermal analysis, infrared and Raman spectroscopy are powerful methods employed in the characterization of hydrotalcite-type materials [2]. The effect of reagent addition on the purity and crystallinity of the hydrotalcite materials showed that adding the base (NaOH) to the acid, proceeding via an acidic pathway, favors the formation of the hydrotalcite. Under strong alkaline conditions, ZnO species are not soluble and are found to compete with the formation of Zn/Al hydrotalcites.

The variation of pH showed that at low pH no hydrotalcite-type structure formed and that with increasing pH, up to pH ~12, the crystallinity also increased. However, at high alkaline pH (14) ZnO forms, probably from the redissolution of the hydrotalcite materials formed at lower pH. Furthermore, the stability of these compounds was observed to increase with increasing pH.

Comparing hydrothermal samples showed that treatment of unstable, confirmed by STEM and thermal analysis, hydrotalcites favors the formation of ZnO and other non-hydrotalcite phases. Where stable, starting materials produce highly crystalline hydrotalcite-type products, which maintain the classical hexagonal-shaped particle.

Acknowledgments

The authors thank Tony Raftery for assistance with X-ray diffraction. Sharyn Price, of the Natural Resources Facility at QUT, is acknowledged for her assistance with the elemental analysis using ICP-OES. Thor Bostrom, of the Analytical Electron Microscopy Facility at QUT, is thanked for his assistance with the STEM analytical phase analysis. The contribution of Shane Russell with the DTA/TGA is greatly appreciated. The financial and infrastructural support of the QUT, Inorganic Materials Research Program, is gratefully acknowledged.

References

[1] F. Trifirò, A. Vaccari, in: T. Bein (Ed.), Comprehensive Supramolecular Chemistry, Vol. 7, Pergamon, Oxford, 1996, p. 251.
[2] W.T. Reichle, Solid State Ion. 22 (1986) 135.
[3] A. Vaccari, Catal. Today 41 (1998) 53.
[4] M.K. Titulaer, J.B.H. Jansen, J.W. Geus, Clays Clay Miner. 42 (1994) 249.
[5] M. Badreddine, M. Khaldi, A. Legrouri, A. Barroug, M. Chaouch, A.D. Roy, J.P. Besse, Mater. Chem. Phys. 52 (1998) 235.
[6] F.M. Labajos, V. Rives, M.A. Ulibarri, J. Mater. Sci. 27 (1992) 1546.
[7] S. Miyata, Clays Clay Miner. 23 (1975) 369.
[8] S. Miyata, Clays Clay Miner. 28 (1980) 50.
[9] F. An, Huagong Keji 11 (2003) 35.
[10] M. Badreddine, A. Legrouri, A. Barroug, A. De Roy, J.-P. Besse, Collect. Czech. Chem. Commun. 63 (1998) 741.
[11] U. Costantino, F. Marmottini, M. Nocchetti, R. Vivani, Eur. J. Inorg. Chem. (1998) 1439.
[12] A. Ennadi, A. Legrouri, A. de Roy, J. Pierre Besse, J. Mater. Chem. 10 (2000) 2337.
[13] J.W. Boclair, P.S. Braterman, Chem. Mater. 11 (1999) 298.
[14] M. Badreddine, M. Khaldi, A. Legrouri, A. Barroug, M. Chaouch, A. de Roy, J.P. Besse, Mater. Chem. Phys. 52 (1998) 235.
[15] M. Badreddine, A. Legrouri, A. Barroug, A. de Roy, J.P. Besse, Mater. Lett. 38 (1999) 391.
[16] L.F. da Silva, J. Tronto, H.P. Oliveira, J.B. Valim, J. Inclusion Phenom. Macrocyclic Chem. 46 (2003) 187.
[17] D.P. Das, J. Das, K. Parida, J. Colloid Interf. Sci. 261 (2003) 213.
[18] M. Guenane, C. Forano, J.P. Besse, Mater. Sci. Forum 152–153 (1994) 343.
[19] J.L. Guimaraes, R. Marangoni, L.P. Ramos, F. Wypych, J. Colloid Interf. Sci. 227 (2000) 445.
[20] E. Kanezaki, J. Mater. Sci. 30 (1995) 4926.
[21] E. Kanezaki, J. Inclusion Phenom. Macrocyclic Chem. 46 (2003) 89.
[22] F. Kooli, W. Jones, Inorg. Chem. 34 (1995) 6237.
[23] F. Kooli, C. Depege, A. Ennaqadi, A. de Roy, J.P. Besse, Clays Clay Miner. 45 (1997) 92.
[24] S. Velu, V. Ramkumar, A. Narayanan, C.S. Swamy, J. Mater. Sci. 32 (1997) 957.
[25] A. Andreev, V. Kafedzhiiski, T. Khalachev, B. Kunev, M. Kalchev, Appl. Catal. 78 (1991) 199.
[26] K. Bahranowski, R. Dula, M. Gasior, M. Labanowska, A. Michalik, L.A. Vartikian, E.M. Serwicka, Appl. Clay Sci. 18 (2001) 93.

[27] S. Bhattacharjee, J.A. Anderson, Chemical Communications, Cambridge, UK, 2004, p. 554.

[28] A. Cervilla, A. Corma, V. Fornes, E. Llopis, P. Palanca, F. Rey, A. Ribera, J. Am. Chem. Soc. 116 (1994) 1595.

[29] J. Das, K. Parida, React. Kinet. Catal. Lett. 69 (2000) 223.

[30] Y.-H. Ge, W.-M. Lu, J.-X. Mao, Wuji Huaxue Xuebao 18 (2002) 1143.

[31] A.H. Padmasri, A. Venugopal, V. Durga Kumari, K.S. Rama Rao, P. Kanta Rao, J. Mol. Catal. A 188 (2002) 255.

[32] R. Zhao, C. Yin, H. Zhao, C. Liu, Fuel Process. Technol. 81 (2003) 201.

[33] J.T. Kloprogge, R.L. Frost, Phys. Chem. Chem. Phys. 1 (1999) 1641.

[34] B. Houri, A. Legrouri, A. Barroug, C. Forano, J.P. Besse, Collect. Czech. Chem. Commun. 63 (1998) 732.

[35] C.F. Baes, R.E. Mesmer, The Hydrolysis of Cations, Wiley, New York, 1976.

[36] S. Velu, V. Ramkumar, A. Narayanan, C.S. Swamy, J. Mater. Sci. 32 (1997) 957.

[37] H. Roussel, V. Briois, E. Elkaim, A. de Roy, J.-P. Besse, J.-P. Jolivet, Chem. Mater. 13 (2001) 329.

[38] H. Roussel, V. Briois, E. Elkaim, A. de Roy, J.P. Besse, J. Phys. Chem. B 104 (2000) 5915.

[39] E.C. Kruissink, L.L.V. Reijen, J.R.H. Ross, J. Chem. Soc. Faraday Trans. I 77 (1981) 649.

[40] M. Lal, A.T. Howe, J. Solid State Chem. 39 (1981) 368.

[41] N. Gutmann, B. Müller, J. Solid State Chem. 122 (1996) 214.

[42] S. Yun, T.J. Pinnavaia, Inorg. Chem. 35 (1996) 6853.

[43] V. Rives, in: V. Rives (Ed.), Layered Double Hydroxides: Present and Future, Nova Science Publishers Inc., New York, 2001, p. 115.

[44] J.T. Kloprogge, J. Kristof, R.L. Frost, in: E.A. Dominguez, G.R. Mas, F. Cravero (Eds.), A Clay Odyssey, Proceedings of the 12th International Clay Conference, Elsevier, Bahia Blanca, Argentina, 2001, p. 451.

[45] F.M. Labajos, V. Rives, M.A. Ulibarri, J. Mater. Sci. 27 (1992) 1546.

[46] S. Morpurgo, M.L. Jacono, P. Porta, J. Solid State Chem. 122 (1995) 324.

[47] W. Kagunya, R. Baddour-Hadjean, F. Kooli, W. Jones, Chem. Phys. 236 (1998) 225.

[48] J.T. Kloprogge, R.L. Frost, in: V. Rives (Ed.), Layered Double Hydroxides: Present and Future, Nova Science Publishers, Inc., New York, 2001, p. 139.

[49] V. Farmer, The Infrared Spectra of Minerals, Mineralogical Society, England, 1974.

[50] K. Nakamoto, Infrared and Raman Spectra of Inorganic and Coordination Compounds, fifth ed., Wiley, USA, 1997.

[51] J.A. Gadsden, Infrared Spectra of Minerals and Related Inorganic Compounds, Butterworths, England, 1975.

[52] B. Schrader, Infrared and Raman Spectroscopy: Methods and Applications, Weinheim, New York, 1995.

[53] S.D. Ross, Inorganic Infrared and Raman Spectra, McGraw-Hill Book Company, London, 1972.

[54] W.T. Reichle, S.Y. Kang, D.S. Everhardt, J. Catal. 101 (1986) 352.